Journal of
Materials Chemistry C

ROYAL SOCIETY
OF CHEMISTRY

PAPER

View Article Online
View Journal | View Issue

Cite this: *J. Mater. Chem. C*, 2025, 13, 20269

Terahertz spectroscopic characterization of $Ge_3Sb_2Te_6$ compounds for active applications

Krishna Kumar, *[ab] Miroslavna Kovylina,[a] Jose Antonio Álvarez-Sanchis,[a] David Ortiz de Zárate,[a] Borja Vidal[a] and Carlos García-Meca[c]

Received 24th April 2025,
Accepted 31st August 2025

DOI: 10.1039/d5tc01667c

rsc.li/materials-c

A study of the optical and dielectric properties of the non-volatile chalcogenide phase change material $Ge_3Sb_2Te_6$ in the terahertz band (0.5–2.5 THz) is presented. Thermally annealed thin films of this material have been characterized with THz time-domain spectroscopy (THz-TDS), in addition to X-ray diffraction (XRD) and Raman spectroscopy. Optical constants, dielectric properties, and THz conductivity were derived from the THz-TDS data using a numerical method that takes into account the strong etalon effect of the thin film. The results are compared to the properties of $Ge_2Sb_2Te_5$, which is commonly employed in photonics. Remarkably, $Ge_3Sb_2Te_6$ exhibits considerably lower losses along the metal-to-insulator (MIT) transition. It has also been found that $Ge_3Sb_2Te_6$ is more robust and that its optical constants are less affected by the substrate material. These results suggest that $Ge_3Sb_2Te_6$ is potentially a more suitable candidate for high-performance applications requiring high contrast in the refractive index and low loss, such as in THz beam steering.

1 Introduction

Chalcogenide phase change materials (ChPCM) composed of germanium (Ge), antimony (Sb) and tellurium (Te) with various stoichiometries exhibit remarkable tunability in their optical, electrical, and dielectric properties.[1,2] These materials exhibit non-volatile highly stable intermediate phases in addition to the amorphous (dielectric, low-loss) and the crystalline (metallic, high-loss) states,[1] reachable upon external stimuli, making them promising candidates for reconfigurable photonic applications.[3–5] This metal-to-insulator transition (MIT), which induces significant optical contrast, arises from the rearrangement of chemical bonds, from covalent bonding in the amorphous state to resonant bonding in the crystalline state.[6] However, the optical constants of these compounds depend on the material stoichiometry[1] and fabrication conditions.[7]

Among these PCMs, $Ge_2Sb_2Te_5$ has been extensively studied and widely applied.[8,9] However, across the literature, its optical and dielectric properties vary significantly.[8–11] Although the phase transitions in $Ge_2Sb_2Te_5$ are ultra-fast (typically 1 ns) and stable for up to 10 years, the material exhibits high losses upon thermal annealing and cannot be annealed at temperatures exceeding 320 °C,[8] limiting the achievable optical contrast. This has driven the search for alternative materials that can reach higher optical contrast with lower losses. Recent studies suggest that similar compounds such as $Ge_3Sb_2Te_6$, $Ge_1Sb_2Te_4$, $Ge_1Sb_4Te_7$, Sb_2Se_3, and Sb_2S_3 exhibit promising characteristics in the optical region,[12–17] but have yet to be explored in the THz domain.

To address this gap, we investigate here the thermally induced electromagnetic properties associated with the MIT transition in the non-volatile chalcogenide compound $Ge_3Sb_2Te_6$. To this end, we used a combination of terahertz time-domain spectroscopy (THz-TDS), X-ray diffraction (XRD), and Raman spectroscopy, with a particular focus on the potential of this material for next-generation programmable THz technologies. We compare the results with the properties of $Ge_2Sb_2Te_5$. THz-TDS is employed to directly measure the time-domain electric field response, providing critical insights into conductivity changes associated with phase transitions in thermally annealed thin films deposited on thick substrates. XRD analysis identifies thermally induced phases and their degree of crystallinity. Raman spectroscopy tracks microstructural changes related to molecular vibrations. In addition, we examine the influence of substrate selection on the optical and dielectric properties of $Ge_3Sb_2Te_6$ across its amorphous, crystalline, and intermediate (mixture-phase) states. The combination of these techniques offers a comprehensive understanding of the temperature-induced structural, optical and electronic transitions in $Ge_3Sb_2Te_6$, advancing its potential for active THz photonic applications.

2 Materials and methods

2.1 Preparation of chalcogenide compounds

Thin films of $Ge_3Sb_2Te_6$ and $Ge_2Sb_2Te_5$ were deposited on 625 ± 25 μm-thick highly resistive silicon (HR-Si) substrates

---

[a] *Nanophotonics Technology Center, Universidad Politecnica de Valencia, Valencia, Spain. E-mail: krishnacelos.isp@gmail.com*
[b] *DAS Photonics, S.A., Valencia 46022, Spain*
[c] *Monodon, Navantia, S.A., S.M.E., Madrid 28005, Spain*

and 450 ± 25 μm sapphire (Al_2O_3) substrates *via* electron beam (e-beam) evaporation using stoichiometric targets of the respective chalcogenide compounds. The reason for using two different substrates was to systematically assess how the substrate material influences the optical constants of the PCMs under study, as it is known that it may affect film growth, crystallinity, and measurements. For instance, the complex refractive index of $Ge_2Sb_2Te_5$ deposited on sapphire was estimated to be 25 + 5i at 260 °C and 21 + 1i at 180 °C,[9] whereas for $Ge_2Sb_2Te_5$ on a quartz substrate, reported values were 18 + 13i at 260 °C and 10 + 2i at 180 °C,[8] all measured at 1 THz.

Prior to deposition, the substrates were cleaned using acetone, ethanol, and O_2 plasma treatments. The evaporation process was carried out at a 4 kV high voltage and a 2.5 mA current under vacuum conditions, with a base pressure of $2–3 \times 10^{-7}$ mbar and a working pressure of $0.3–3 \times 10^{-6}$ mbar. The deposition rate was monitored using a water-cooled quartz crystal microbalance. The thin films were measured *via* profilometry (DEKTAK XT), which determined a thickness approximately 110 nm ± 10 nm.

To ensure accurate extraction of the optical properties, which depend on the THz transmission ratio between the sample (thin film + substrate) and the bare substrate,[8,9,18] only half of each substrate was coated with the GST thin film, while the other half was left uncoated for reference. Post-deposition, each sample was annealed at different temperatures: 155 °C, 205 °C, 255 °C, 305 °C, 355 °C, and 405 °C, to induce various crystalline phases.

The material composition of the fabricated GST films was verified by scanning electron microscope energy dispersive X-ray (SEM-EDX) measurements. To this end, we used a field emission scanning electron microscope (FE-SEM Joel IT1800 SHL) with a fully embedded energy dispersive X-ray spectrometer (EDS), operated at beam energies ranging from 10 and 30 kV and probe currents from 0.20 to 5.65 nA. As a result, we obtained a measured composition of $Ge_{2.9}Sb_2Te_{6.1}$ for nominal $Ge_3Sb_2Te_6$ and $Ge_{1.7}Sb_{2.2}Te_{5.1}$ for nominal $Ge_2Sb_2Te_5$, both of which were found to remain stable post annealing, supporting the results of our study.

The uniformity of thin films post-annealing was confirmed through Raman spectroscopy at three different spatial locations on each sample and by optical imaging, which shows no sign of degradation for $Ge_3Sb_2Te_6$, whereas spatial non-uniformity was observed for $Ge_2Sb_2Te_5$ samples annealed above 305 °C (as shown in Fig. 1). Thermally induced MIT transitions were analyzed through XRD and Raman spectroscopy, as detailed in the subsequent sections.

2.2 XRD

The XRD patterns of $Ge_3Sb_2Te_6$ and $Ge_2Sb_2Te_5$ thin films, both deposited on silicon substrates and annealed at a temperature of 155 °C, 205 °C, 255 °C, and 305 °C, as well as in the as-grown state, are presented in Fig. 2. Highly intense and broad diffraction peaks corresponding to the HR-Si substrate were observed around $2\theta = 14°$ (not shown in Fig. 1), where 2θ is the angle between the incident X-ray beam and the diffracted beam.

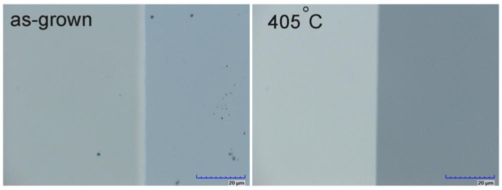

(a) $Ge_3Sb_2Te_6$ on silicon

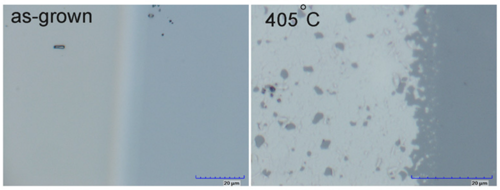

(b) $Ge_2Sb_2Te_5$ on silicon

Fig. 1 Optical images of as-grown and annealed (at 405 °C) samples of (a) $Ge_3Sb_2Te_6$ and (b) $Ge_2Sb_2Te_5$, both deposited on HR-Si substrate. Scale bar: 20 μm.

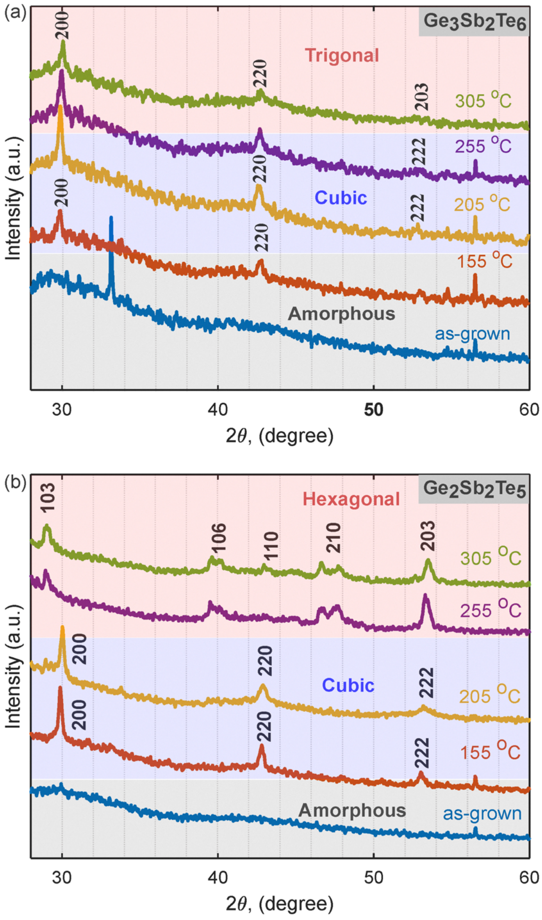

Fig. 2 X-ray diffraction (XRD) patterns of (a) $Ge_3Sb_2Te_6$ and (b) $Ge_2Sb_2Te_5$ compounds, recorded at annealing temperatures of 155 °C, 205 °C, 255 °C, and 305 °C. The observed diffraction peaks correspond to the characteristic reflections associated with the amorphous and crystalline phases of these materials. These results indicate a transition from an insulating to a metallic state as thermal annealing progresses. The peak assignment was made in accordance with reported literature data,[1,8,9,21] providing insight into the structural transformations induced by annealing.

For the as-grown films, only a broad peak was observed around 2θ = 30°, indicating an amorphous[9] or partially disordered phase.[1] In contrast, distinct diffraction peaks emerged in the annealed films, reflecting the structural changes associated with the phase transition at higher temperatures.

For the common $Ge_2Sb_2Te_5$ (Fig. 2b) samples annealed between 155 °C and 205 °C, the broader peak around 2θ = 30° (corresponding to the crystallographic plane 200) grows sharply indicating the presence of face-centered cubic (FCC) phases. In samples annealed above 205°, new peaks appear at lower 2θ values (103), corresponding to the development of hexagonal close-packed (HCP) phases.[8,9] In contrast, $Ge_3Sb_2Te_6$ (Fig. 2a) exhibited a slightly different thermal response. The broader peak at 30° (200) grows slowly compared to $Ge_2Sb_2Te_5$, suggesting a higher transition temperature from as-grown to cubic phases in $Ge_3Sb_2Te_6$.[1] In addition, no new peak evolution was detected near 30° for samples annealed up to 205 °C. However, samples annealed above 255 °C showed new peaks at higher 2θ values, slightly higher than 30°, indicating the coexistence of mixed (FCC and trigonal) crystalline phases. This kind of coexistence of different phases within the same PCM can be understood from the following fact. As the annealing temperature of an as-grown sample is increased towards the amorphous–crystalline phase change temperature, small crystalline nuclei are formed in the amorphous matrix, and these nuclei grow to eventually make the material fully crystalline. For annealing temperatures between those associated with the initiation and completion of crystallization, the material exists as a mixture of two different phases (phase coexistence). If uniform heating is applied, these intermediate states involve crystalline precipitates uniformly dispersed throughout an amorphous matrix.[7,19] In this situation, the material behaves as an effective homogeneous medium whose optical properties are approximately a weighted average of those associated with the purely amorphous and crystalline phases, with weights that depend on the degree of crystallization (which in turn depends on the annealing temperature).[20] Something similar happens between two crystalline phases.[19]

Secondary peaks emerged at 43° (220) and 53° (222) for samples annealed at 155 °C and 205 °C, respectively. These correspond to the formation of cubic phases in both $Ge_3Sb_2Te_6$ and $Ge_2Sb_2Te_5$ samples.[1,8,9] For $Ge_2Sb_2Te_5$ samples annealed above 205 °C, additional peaks around 40° (106) and 47° (210) appeared, indicating the formation of HCP lattices. In contrast, the XRD peaks of $Ge_3Sb_2Te_6$ samples grow slowly compared to those of $Ge_2Sb_2Te_5$. The samples annealed above 205 °C showed a distinct behavior, with the emergence of a peak around 53° (222) without any additional peaks near 40° and 47°. These differences in the rate of growth of XRD peaks with annealing temperature indicate different crystallization pathways in addition to the different crystallization phases of $Ge_2Sb_2Te_5$ and $Ge_3Sb_2Te_6$. These observations were found to be consistent with previous studies of similar materials.[1,8,9,21]

2.3 Raman analysis

To further investigate the phase transitions linked to thermally-induced microstructural changes in $Ge_3Sb_2Te_6$ thin films and compare its features with those of $Ge_2Sb_2Te_5$, Raman spectra were measured for samples annealed at 155 °C, 205 °C, 255 °C, 305 °C, and 355 °C, as shown in Fig. 3. Raman spectra were obtained using a Jobin Yvon T64000 triple spectrometer equipped with a laser operating at 785 nm, and a grating of 600 gr mm^{-1}, allowing spectral data collection over a range of 50 to 250 cm^{-1} with a resolution of 3.03 cm^{-1}.

No Raman peaks were observed from the HR-Si substrate within the recorded range, while both the as-grown (amorphous) and annealed (crystalline) thin films showed broad spectral envelopes, which is an indication of overlapping of multiple peaks. However, distinct features within these envelopes were identified that show similarities with earlier reported literature for $Ge_3Sb_2Te_6$[4,22,23] and $Ge_2Sb_2Te_5$.[8,22,24,25] In $Ge_2Sb_2Te_5$, these bands originate due to transitions from amorphous to cubic and

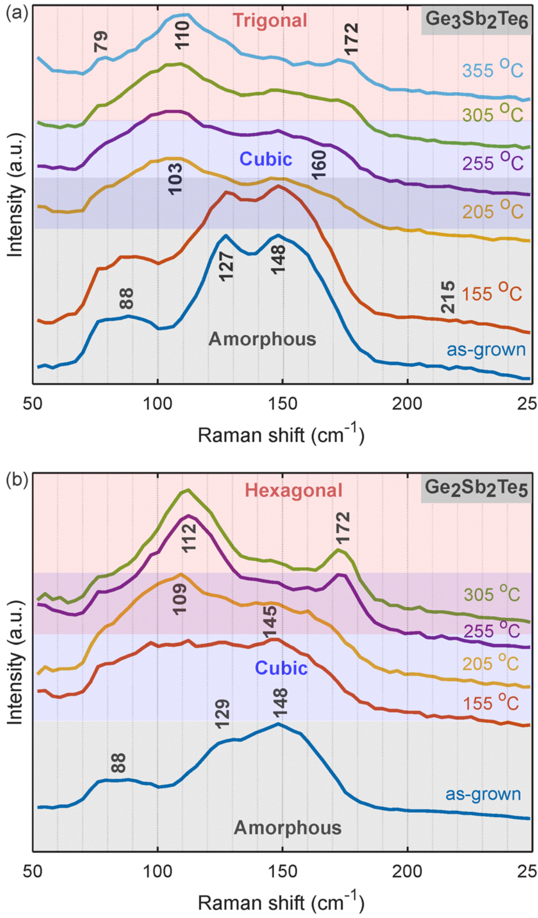

Fig. 3 Raman spectra of (a) $Ge_3Sb_2Te_6$ and (b) $Ge_2Sb_2Te_5$ compounds, recorded at annealing temperatures of 155 °C, 205 °C, 255 °C, 305 °C and 355 °C (only for $Ge_3Sb_2Te_6$). The Raman spectrum of $Ge_2Sb_2Te_5$ annealed at 355 °C is not shown. The broad spectral envelope arises from the superposition of multiple peaks associated with lattice vibrational modes, whereas shifts in the envelope peak with increasing annealing temperature reflect thermally induced microstructural changes, signifying the transition from the as-grown amorphous phase to a crystalline state. The observed Raman modes are consistent with the vibrational modes previously reported in the literature,[4,8] further supporting the structural evolution of the materials with thermal annealing.

then to hexagonal phases with increasing annealing temperature,[8,9] and in $Ge_3Sb_2Te_6$ due to transitions from amorphous to cubic and subsequently to trigonal phases.[4,26]

Specifically, the as-grown amorphous $Ge_2Sb_2Te_5$ film shows three distinct spectral bands [Fig. 3(b), blue curve]. A low intensity Raman band around 88 cm^{-1} can be attributed to the Sb–Sb bonds vibrations in $Te_2Sb–SbTe_2$,[22] or to the E-modes of $GeTe_4$.[27] The second and the most dominant band appears near 150 cm^{-1}, can be attributed to the Sb–Te vibrations in $SbTe_3$ pyramidal units[22,28] or potentially from the defective octahedra co-ordination of Sb atoms.[29,30] The third peak, near 129 cm^{-1}, corresponds to the A_1 mode of $GeTe_{4-n}Ge_n$ ($n = 1, 2$), related to the corner sharing $GeTe_4$ tetrahedra modes.[31,32] This peak may also corresponds to the B-band of vibrational modes in a-GeTe.[27] Similarly, the as-grown amorphous $Ge_3Sb_2Te_6$ films show three distinct spectral bands with slightly shifted frequencies and different peak strengths [Fig. 3(a), blue curve], consistent with the findings reported by K. Shportko *et al.*[23] Compared to the as-grown amorphous $Ge_2Sb_2Te_5$, the first band near 88 cm^{-1} appears stronger and can be attributed to the $\Gamma_3(E)$ vibrational mode, similar to one found in single crystalline α-GeTe.[23] This increase in intensity is likely due to the higher Ge-content in $Ge_3Sb_2Te_6$, which enhances weaker bands around 88 cm^{-1} and 215 cm^{-1} (not clearly visible). Additionally, the second and the third bands near 127 cm^{-1} and 148 cm^{-1} now have similar peak strength, unlike in as-grown amorphous $Ge_2Sb_2Te_5$. Once again, the weak features (near 129 cm^{-1}) of amorphous $Ge_2Sb_2Te_5$ gain intensity due to the increased Ge content in $Ge_3Sb_2Te_6$, which leads to the weakening of the Sb–Te vibrations associated with $SbTe_3$ pyramidal units or the defective octahedral configurations of Sb-atoms.[23]

Upon thermal annealing, the peak near 148 cm^{-1} gradually decreases in intensity for $Ge_2Sb_2Te_5$ samples annealed between 155 °C (orange curve) to 205 °C (yellow curve), indicating a transition to the cubic phase. This peak disappears completely in samples annealed above 205 °C. Instead, two new band emerges at 112 and 172 cm^{-1} (violet and green) similar to those previously observed during the crystallization of Sb_2Te_3 films.[32] These bands may be attributed to bulk Sb_2Te_3, typically the $E_g(2)$ and $A_{1g}(2)$ vibrational modes of the hexagonal phase. Additionally, the 129 cm^{-1} band splits into two weaker closely overlapping bands at 109 cm^{-1} and 145 cm^{-1}. These are due to vibrational modes of the cubic (FCC) crystalline phase and are observed in samples annealed at 155 °C (orange curve) and 205 °C (yellow curve).[32] The band at 109 cm^{-1} can be attributed to the softened A_1 mode of corner-sharing $GeTe_4$ tetrahedra, while the one at 145 cm^{-1} is linked to the A_1 mode of $GeTe_{4-n}Ge_n$ ($n = 1, 2$).

In contrast, for $Ge_3Sb_2Te_6$, the as-grown sample and the one annealed at 155 °C show nearly identical Raman features, except for a weak broadband near 88 cm^{-1} that slightly increases in intensity. This suggests that the crystallization temperature for the amorphous-to-cubic phase transition exceeds 155 °C,[33] likely due to the increase in Ge content in $Ge_3Sb_2Te_6$.

Samples annealed at 205 °C (yellow curve) and 255 °C (violet curve) exhibit nearly identical Raman spectra, though with a reduced intensity of the 148 cm^{-1} band compared to the as-grown sample. In addition, two new bands emerge: one clearly visible at 103 cm^{-1} and another broad one near 160 cm^{-1}, indicating the transition to the characteristic metastable cubic phase.[4] The 103 cm^{-1} band can be assigned to the E_g mode and the 160 cm^{-1} to the A_{1g} mode.[34]

Annealing above 255 °C causes further reduction in the 148 cm^{-1} band, with the most significant decrease observed at 355 °C. Meanwhile, the band at 103 cm^{-1} becomes narrower while maintaining its peak intensity in samples annealed at 305 °C and shifts towards higher frequencies in those annealed at 355 °C. At 355 °C, the Raman spectrum exhibits three characteristic bands: a nearly resolved peak at 79 cm^{-1}, another near 110 cm^{-1} and a third at 172 cm^{-1}.[4] These can be attributed to the E mode of α-GeTe,[23] the A_1 mode of $GeTe_6$[35] and the $A_{1g}(2)$ mode of Sb_2Te_3, respectively. The latter may be linked to vacancy ordering into layers, which breaks the local symmetry and transforms into van der Waals gaps as the trigonal phase forms.

2.4 THz spectroscopic data processing

The transient electric fields transmitted through the sample (thin film + substrate, $E_{\text{sample}}(t)$) and the bare substrate ($E_{\text{substrate}}(t)$) used as reference were measured using an in-house-built all-fiber THz-TDS spectrometer based on a femtosecond laser (Toptica FemtoFErb 1560) at 1550 nm and photoconductive switches (MENLO TERA15). The time-domain scanning was performed with a voice coil optical delay line with an approximate range of 50 ps at a speed of 5 traces per s. Measurements were performed in a laboratory at 25 °C with dry air (humidity < 10%) purged in the propagation path to eliminate the effects of water vapor, *i.e.*, ringing after the main THz pulse in the time domain, resulting in sharp absorption lines in the spectra. The optical properties of the material were derived from the transfer function. This transfer function is defined as the ratio of the Fourier transforms of $E_{\text{sample}}(t)$ and $E_{\text{substrate}}(t)$, allowing for analysis in the frequency domain. Because of the finite thickness of both the thin film and the substrate, etalon effects were observed, producing interference patterns in the measured transmission spectra.

To mitigate substrate-induced etalon effects, a Tukey apodization filter with a width of 18 ps and a smoothness parameter of 0.9 was applied during the post-processing. However, it does not remove the etalon effect of the thin film, given its small thickness in terms of the THz wavelength λ_{THz}, which results in the etalon response overlapping with the main pulse. This effect can be taken into account by the transfer function:[18,36]

$$T(\omega) = \frac{2N(n_{\text{sub}}+1)e^{i\omega\frac{d(N-n_{\text{sub}})}{c}}}{(1+N)(n_{\text{sub}}+N)+(n_{\text{sub}}-N)(N-1)e^{2i\omega\frac{dN}{c}}}, \quad (1)$$

where ω is the agular frequency, N is the complex refractive index of the thin film, n_{sub} is the refractive index of the substrate, d is the thin-film thickness, and c is the speed of light in vacuum.

To determine the complex refractive index N from the experimentally measured transfer function, $T(\omega)$, the above equation can be solved, either analytically under the thin-film approximation,[37] or numerically.[8] Analytical solutions rely on the assumptions $d \ll \lambda_{\mathrm{THz}}$, corresponding to the conditions $|n\omega d/c| \ll 1$ and $|n_{\mathrm{sub}}\omega d/c| \ll 1$.[38] While these approximations are valid for thin films on thick substrates, they may not hold for high-refractive-index n thin-films with significant optical contrast, where $|n\omega d/c|$ approaches unity, rendering the thin-film approximation unreliable.

To address this challenge, we numerically solve the equation for $T(\omega)$ using the MATLAB fsolve function, enabling precise determination of N. From N, the dielectric permittivity ε can be calculated as $\varepsilon = N^2$.

The extracted optical constants were further validated by simulating the transmission function using CST Microwave Studio (MWS) and comparing the results with the experimental data. The simulation results showed excellent agreement with the measured transmission spectra.

3 Results

3.1 Transmittance

Fig. 4 shows the transmittance spectra of $Ge_2Sb_2Te_5$ and $Ge_3Sb_2Te_6$ thin films within the frequency range of 0.5–2.5 THz at increasing annealing temperatures.

The transmittance decreases monotonically with increasing annealing temperature, exhibiting a rather flat response over the measured frequency range. However, the reduction in transmittance is more pronounced for $Ge_2Sb_2Te_5$ as compared to $Ge_3Sb_2Te_6$. $Ge_2Sb_2Te_5$ demonstrates a more significant drop in transmittance with increasing annealing temperature, approaching nearly 15% transmittance for $Ge_2Sb_2Te_5$ on Al_2O_3 (plus, purple) and nearly 5% for $Ge_2Sb_2Te_5$ on silicon (cross, purple) for samples annealed at 255 °C. Further annealing $Ge_2Sb_2Te_5$ samples does not alter the transmittance and it remains same, nearly 5% (cross, cyan). In contrast, approximately 75% transmittance is observed for $Ge_3Sb_2Te_6$ annealed at 255 °C (star and circle, purple) and nearly 10% transmittance for the sample annealed at 405 °C (circle, red). We have considered $Ge_2Sb_2Te_5$ annealed up to 355 °C and $Ge_3Sb_2Te_6$ up-to 405 °C, for which the transmittance is above 5%.

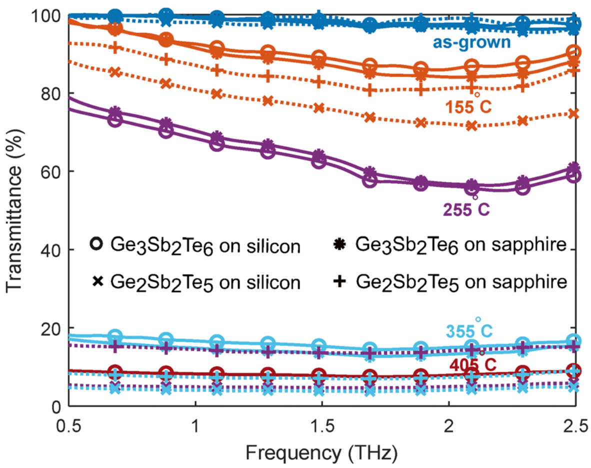

Fig. 4 THz-transmittance spectra of $Ge_3Sb_2Te_6$ (110 ± 10 nm, solid curve with circles) and $Ge_2Sb_2Te_5$ (110 ± 10 nm) deposited on a silicon substrate (dashed curve with crosses), as well as $Ge_3Sb_2Te_6$ (115 ± 10 nm, solid curve with stars) and $Ge_2Sb_2Te_5$ (95 ± 10 nm, dashed curve with plus signs) deposited on Al_2O_3 substrates, were measured over a broad frequency range of 0.5–2.5 THz using a THz-TDS instrument. The spectra of each sample were recorded following annealing at various temperatures: 155 °C, 205 °C, 255 °C, 305 °C, 355 °C and 405 °C.

3.2 Complex refractive index and permittivity

Fig. 5 presents a comparison between the numerically extracted (solid lines) and analytically extracted (dashed lines) complex refractive indices of $Ge_3Sb_2Te_6$. Both indices closely overlap for the as-grown sample and those annealed up to 255 °C closely. However, the analytical method tends to overestimate the real part of the refractive index for the sample annealed at 405 °C (by 9.5% at 1 THz) and the imaginary part for the sample annealed at 355 °C (by 9% at 1 THz). This suggests that the

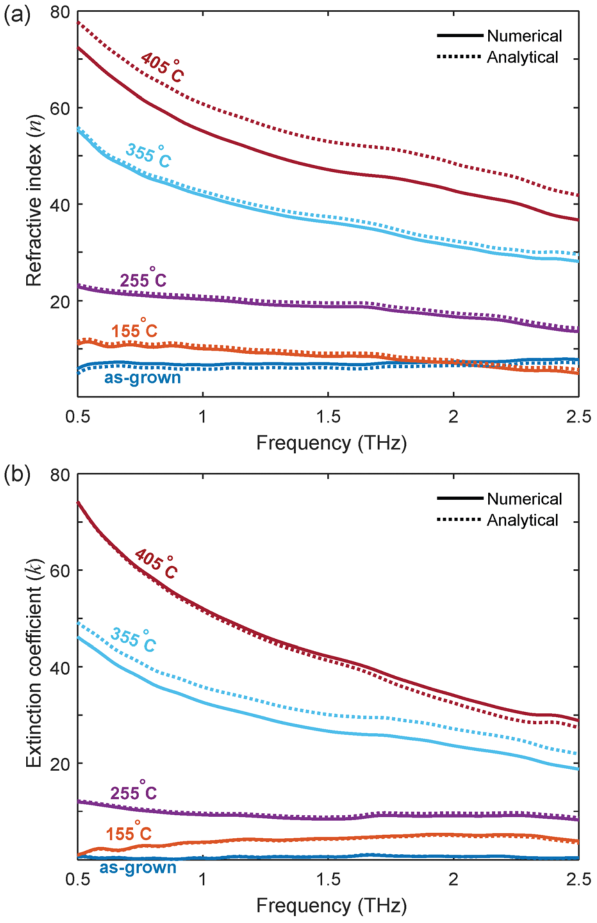

Fig. 5 A comparison of numerically and analytically extracted (a) refractive index, n, and (b) extinction coefficient, k, is presented for $Ge_3Sb_2Te_6$ thin films deposited on a silicon substrate.

analytical solution is more reliable for thin films with lower refractive indices, although both methods yield similar results. Therefore, for further analysis, we consider only the numerically extracted values.

Fig. 6 illustrates the extracted values for (a) the refractive index (real part of), *n*, and (b) the extinction coefficient, *k*, of thermally annealed GST thin films, with $N = n + ik$ being the material complex refractive index (see SI1, SI, for a comparison of these data with the optical constants of $Ge_2Sb_2Te_5$ reported in previous works at 1 THz). An exponential increase in *n* at lower frequencies strongly suggests a metallic behavior for $Ge_3Sb_2Te_6$ samples annealed above 255 °C, as well as for $Ge_2Sb_2Te_5$ samples annealed above 155 °C. For $Ge_3Sb_2Te_6$ films deposited on silicon and Al_2O_3 substrates, the refractive index curves overlap throughout the annealing temperature range, suggesting that the choice of substrate has no significant effect on the optical properties of this material. In contrast, a slight difference is observed for $Ge_2Sb_2Te_5$, consistent with earlier findings reported in the literature.[8–11] Specifically, $Ge_2Sb_2Te_5$ deposited on silicon shows a faster rate of increase in the refractive index compared to the same material deposited on a Al_2O_3 substrate. Furthermore, when comparing the two composites, $Ge_2Sb_2Te_5$ exhibits a sharper increase in refractive index compared to $Ge_3Sb_2Te_6$ on both silicon and Al_2O_3.

$Ge_3Sb_2Te_6$ exhibits a lower thermo-optic coefficient – defined as the rate of change of refractive index with respect to temperature (dn/dT) – compared to $Ge_2Sb_2Te_5$. For example, at 1 THz, the refractive index of $Ge_2Sb_2Te_5$ increases sharply from 16 in its as-grown state to 60 at an annealing temperature of 255 °C, while $Ge_3Sb_2Te_6$ shows a more gradual increase, rising from 6.5 to 52 at 405 °C (see inset in Fig. 6a). The higher thermo-optic coefficient of $Ge_2Sb_2Te_5$ makes it well suited for frequency-agile terahertz applications that require a shift in the resonance frequency. However, this high thermo-optic coefficient in $Ge_2Sb_2Te_5$ is accompanied by a large thermal extinction coefficient – defined as the rate of change of the extinction coefficient with respect to temperature (dk/dT). This large thermal extinction coefficient (see inset in Fig. 6b) can be a drawback in applications where it is important to shift the resonance frequency without affecting the resonance strength, for instance, in beam steering using phase-arrayed antennas.

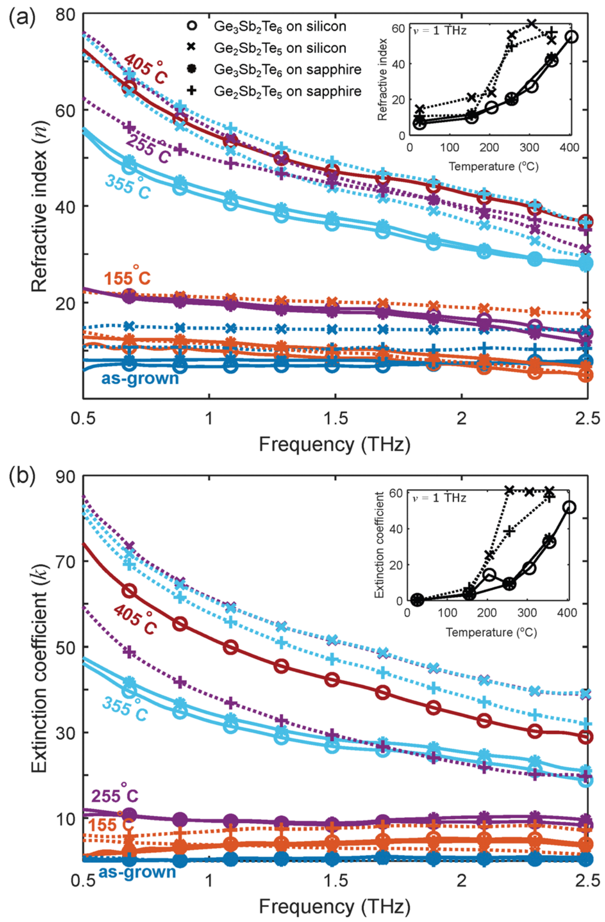

Fig. 6 Numerically extracted (a) refractive index, *n*, and (b) extinction coefficient, *k*, are presented for thin films of $Ge_3Sb_2Te_6$ deposited on Si (solid curve with circles), $Ge_2Sb_2Te_5$ on Si (dashed curve with crosses), $Ge_3Sb_2Te_6$ on Al_2O_3 (solid curve with stars), and $Ge_2Sb_2Te_5$ on Al_2O_3 (dashed curve with plus signs) at annealing temperatures of 155 °C, 255 °C, 355 °C and 405 °C.

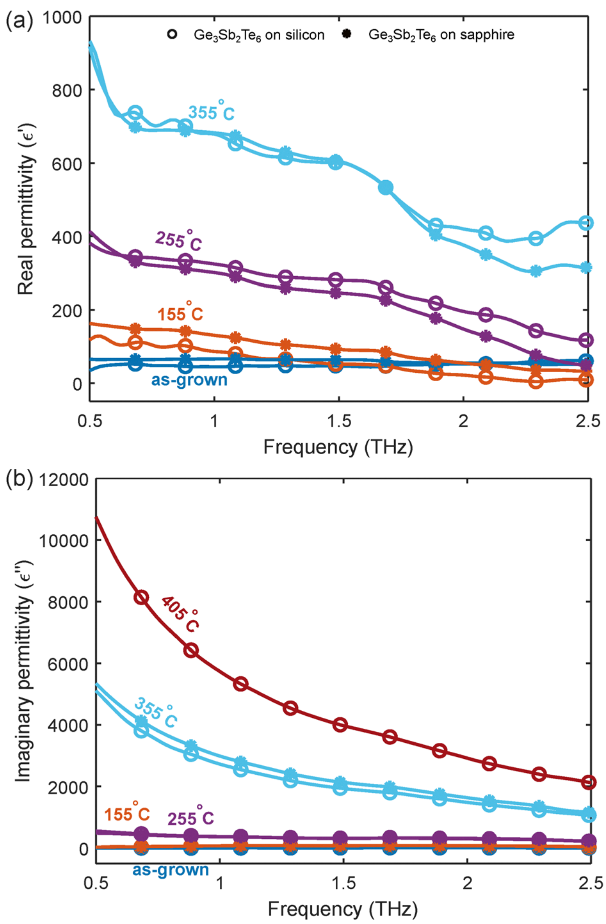

Fig. 7 (a) The real (ε') and (b) imaginary (ε'') components of the dielectric permittivity of $Ge_3Sb_2Te_6$ thin-film, deposited on silicon (solid line with circles) and Al_2O_3 (solid line with stars) substrates, are presented for samples annealed at 155 °C, 255 °C, 355 °C and 405 °C in addition to the as-grown amorphous samples.

In comparison, due to its lower thermo-optic coefficient, $Ge_3Sb_2Te_6$ could serve as a better alternative to $Ge_2Sb_2Te_5$, offering more control over its optical properties within the MIT, which makes it advantageous for THz photonics applications that require a gradual shift in the complex refractive index without significant absorption changes. This enhanced flexibility comes at the cost of a higher annealing temperature.

Another important aspect of the considered materials is the complex dielectric function, which is defined as $\varepsilon = N^2$, where $\varepsilon = \varepsilon' + i\varepsilon''$. The real part of the dielectric function, ε', is given by $\varepsilon' = n^2 - k^2$, and the imaginary part, ε'', is expressed as $\varepsilon'' = 2nk$. The accuracy of ε' is highly dependent on the extracted complex refractive index, which, in turn, relies on the precision of the measured thickness of both the thin film and the substrate. Any slight variation in thickness introduces changes in the extracted refractive index (N), with real and imaginary components becoming $n + \Delta n$ and $k + \Delta k$, respectively. This results in an additional term for the real part of the dielectric function which, to first order, reads:

$$\Delta\varepsilon' \approx 2n\Delta n - 2k\Delta k \tag{2}$$

Since Δn and Δk typically have opposite signs, their contributions combine, leading to significant errors in the calculated real part of the dielectric function.[36,39] For example, as evident from Fig. 6, the n and k curves for the $Ge_3Sb_2Te_6$ samples annealed above 255 °C and the $Ge_2Sb_2Te_5$ samples annealed above 155 °C (corresponding to the crystalline phase of these PCMs), exhibit similar shapes and values, especially in the case of the sample annealed at 405 °C. Therefore, even small errors in n and k (typically less than one unit) can lead to a significant deviation in the calculated value of ε'. As a result, we successfully extracted the complex dielectric permittivity of $Ge_3Sb_2Te_6$ for all annealing temperatures except for 405 °C, for which $n \approx k$ and the values recovered for ε' are not reliable for the reasons mentioned above. Both, $Ge_3Sb_2Te_6$ on silicon and $Ge_3Sb_2Te_6$ on Al_2O_3 samples exhibited similar permittivity magnitudes and trends as depicted in Fig. 7. The results demonstrated an increase in the permittivity with increasing annealing temperatures. The as-grown amorphous sample and the sample annealed at 155 °C showed comparable permittivity values, indicating the dominant amorphous phase of $Ge_3Sb_2Te_6$ at these temperatures. In contrast, the pronounced increase in the permittivity observed for the sample annealed at 255 °C is consistent with a phase transition from the amorphous to the cubic phase at this temperature. A larger increase in permittivity for the sample annealed at 355 °C indicates the coexistence of cubic and trigonal phases in $Ge_3Sb_2Te_6$. To gain deeper insight into the transformation from amorphous (insulating) state to the metallic (crystalline) state, we have investigated the conductive properties of the studied PCMs, as discussed in next section.

4 Conductivity

THz frequencies, with energies comparable to thermal energy, can stimulate the dynamics of charge-carrier quasi-particles, such as free electrons, holes, surface plasmons, excitons, and polaritons, while also triggering collective excitations like optical phonons. To investigate the leading mechanisms underlying charge transport in the considered PCMs, we extracted their THz conductivity from the measured complex refractive index, expressed as $\sigma = i\varepsilon_0\omega N^2 = \sigma' + i\sigma''$, where ε_0 is the permittivity of vacuum. Therefore, the real part of the conductivity σ' depends solely on the imaginary part of the dielectric function ($\sigma' = \varepsilon_0\omega\varepsilon''$). This implies that σ' typically exhibits a lower relative error than σ'' and provides meaningful information on the transition from metal to insulator in thermally annealed samples.[36,39] We calculated σ' for the thermally annealed GST samples, as shown in Fig. 8. In the same way as the transmittance, the extinction coefficient (k), and the imaginary part of the dielectric function (ε''), the THz conductivity of $Ge_3Sb_2Te_6$ demonstrates a gradual increase with increasing annealing temperature. Additionally, the retrieved conductivity values are similar to the ones previously reported for other Ge–Sb–Te chalcogenide compounds.[9,39,40]

To further analyze these observations, the THz conductivity spectra were fitted using a Drude–Lorentz model described by the following equation:

$$\sigma(\omega) = \frac{\sigma_{\mathrm{DC}}}{1 + (\omega\tau)^2} + \sum_{i=1}^{4} \frac{A_i}{(\omega_i - \omega)^2 + \gamma_i^2}, \tag{3}$$

where σ_{DC} represents the DC or static conductivity, and τ is the scattering time associated with the Drude term, which corresponds to the contribution from non-local free charge carriers in the material. The Lorentz term, expressed as a summation over up to 4 Lorentz oscillators, accounts for localized optical phonons oscillating at specific frequencies ω_i with oscillator strength A_i and damping constant γ_i.

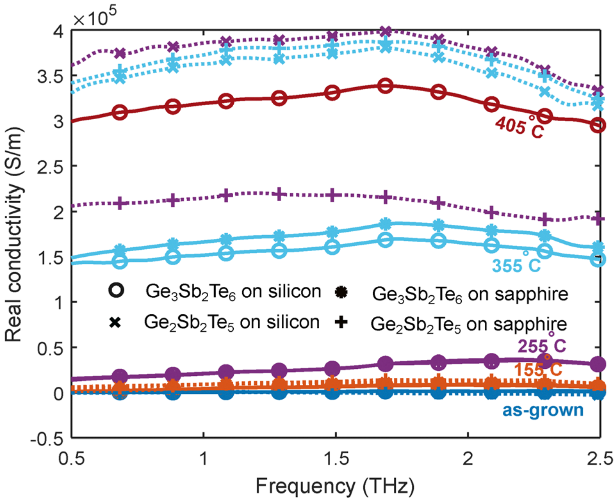

Fig. 8 Numerically extracted real component of THz conductivity for $Ge_3Sb_2Te_6$ deposited on Si (solid curve with circles), $Ge_2Sb_2Te_5$ on Si (dashed curve with crosses), $Ge_3Sb_2Te_6$ on Al_2O_3 (solid curve with stars), and $Ge_2Sb_2Te_5$ on Al_2O_3 (dashed curve with plus signs) at annealing temperatures of 155 °C, 255 °C, 355 °C and 405 °C in addition to the as-grown amorphous samples.

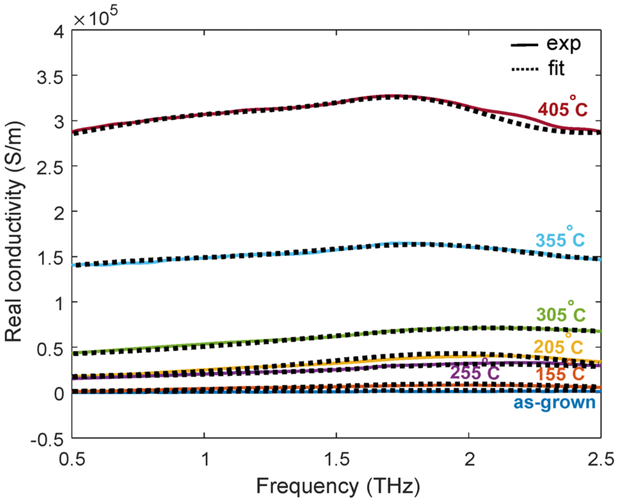

Fig. 9 Drude–Lorentz fitted THz conductivity of $Ge_3Sb_2Te_6$ deposited on Si. Solid lines represent the numerically extracted real part of the THz conductivity (mean values) obtained from THz transmission measurements at three different spots on the sample. Black dashed lines represent Drude–Lorentz model fits.

The numerically extracted real part of the THz conductivity obtained from THz transmission measurements (solid lines) and the Drude–Lorentz fitted THz conductivity (dashed lines) are presented in Fig. 9. The fitting parameters (with error intervals corresponding to standard deviations) for the Lorentz oscillators are summarized in Table 1. Note that the values of σ_{DC} and τ for the as-grown and 155 °C annealed samples are very small, indicating a largely insulating behavior. In these cases, in which the Drude term contributes minimally (it was not possible to calculate the error bar for them for this reason), we used it as a fitting placeholder to capture any residual low-frequency behavior, although its physical interpretation is limited and its omission would hardly alter the results.

To analyze the conductivity behavior of $Ge_3Sb_2Te_6$, we investigated the physical meaning of its DC conductivity values, as obtained from the Drude–Lorentz fits. As shown in Table 1, both the as-grown sample and the one annealed at 155 °C exhibit nearly zero DC conductivity, consistent with their amorphous state. Within this phase, the conductivity exhibits a relatively slow increase with temperature as more carriers are excited,[19] which justifies the slight difference between the as-grown and 155 °C-annealed samples. In contrast, samples annealed above 155 °C show a much more drastic increase in DC conductivity, from near-zero to approximately 10^4 S m^{-1}, typical of the transition to the FCC phase, for which the material experiences the highest conductivity increment (of 2–3 orders of magnitude).[19] The samples annealed at 205 °C and 255 °C exhibit comparable DC conductivity values (also evident from Fig. 9), suggesting they are likely in the same (FCC) structural phase. Further, the sample annealed at 305 °C results in a 2.5× increase in the DC conductivity, of the same order of the 4.4× increase reported for $Ge_2Sb_2Te_5$ in its cubic phase upon annealing from 200 °C to 280 °C, based on Hall measurements.[41] Again, this slower conductivity growth is common within a given phase, although, in crystalline phases, it is due to the increase of mobility (rather than carrier concentrations as in the amorphous phase), as crystal grains grow during heating and the scattering by grain boundaries decreases.[19] At 355 °C and 405 °C, the DC conductivity increases by 12× and 28×, respectively (relative to 255 °C), indicating progression towards the trigonal phase. This overall 28 factor is of the same order of magnitude as that associated with the FCC-hexagonal $Ge_2Sb_2Te_5$ transition.[19] It is also consistent with the 76× increase reported for $Ge_2Sb_2Te_5$ between 180 °C to 400 °C,[41] taking into account that $Ge_3Sb_2Te_6$ requires a higher annealing temperature to achieve a fully trigonal phase (at least over 355 °C in our case) than $Ge_2Sb_2Te_5$ to achieve a fully hexagonal phase (340 °C as reported in ref. 41) together with the fact that optical constants in fully crystalline phases continue to evolve during heat treatment due to vacancy ordering.[7]

In addition, we conducted variable-temperature electrical measurements to further strengthen our study on the MIT transition behavior of the two considered GST compositions and support the presence of phase co-existence in $Ge_3Sb_2Te_6$. In particular, we used an in-line four-point probe (4PP) method[42] to measure the sheet resistance (R_{sh}) of the studied PCMs and calculated the corresponding DC conductivity (σ_{DC}^{4PP}) for both as-grown amorphous and thermally annealed crystalline samples. The full results are included in Table S1 of SI2 (SI) and reveal a significant contrast in R_{sh} between the amorphous and crystalline phases for both compositions, consistent with a clear MIT. For instance, the as-grown amorphous $Ge_3Sb_2Te_6$ film exhibits an extremely high R_{sh} value of $\sim 42 \times 10^6\ \Omega\ \square^{-1}$, while the $Ge_3Sb_2Te_6$ sample annealed at 405 °C shows a drastic reduction in R_{sh} down to $\sim 64\ \Omega\ \square^{-1}$, indicating full crystallization. To further understand the electrical switching behavior, we compared the σ_{DC}^{4PP} of crystalline $Ge_3Sb_2Te_6$ with its DC conductivity inferred from THz-TDS measurements *via* eqn (3) (σ_{DC}^{TDS}). For the as-grown samples, the THz-TDS measurements yielded a negligible conductivity value, in accordance with 4PP measurements. For samples annealed at 405 °C, $\sigma_{DC}^{TDS} \approx 1.51\ \sigma_{DC}^{4PP}$, which is reasonable given that THz-TDS captures both localized and

Table 1 Drude–Lorentz model fitting parameters for $Ge_3Sb_2Te_6$ at different annealing temperatures with error bars (standard deviation)

Annealing temp. (°C)	Thickness (nm)	σ_{DC} (S m^{-1})	τ (ps)	$f_j = \omega_j/2\pi$ (THz)	γ_j (THz)
As-grown	117	2.3×10^{-14}	3.4×10^{-6}	1.85 ± 0.05, 4.57 ± 0.24	4.21 ± 2.67, 19.26 ± 3.52
155	112	4.0×10^{-14}	0.1×10^{-4}	1.22 ± 0.08, 2.05 ± 0.06	4.16 ± 4.11, 21.06 ± 5.64
205	86	10 446 ± 974	0.1164 ± 0.06	1.97 ± 0.02, 3.09 ± 0.02	34.67 ± 5.11, 2.40 ± 0.90
255	112	9166.5 ± 3510	0.0461 ± 0.11	2.09 ± 0.02, 3.63 ± 0.05	35.43 ± 10.12, 17.62 ± 10.67
305	101	22 447.9 ± 8246	0.1015 ± 0.09	2.08 ± 0.07, 3.5 ± 0.01	70.78 ± 24.24, 10.84 ± 1.62
355	111	111 366.5 ± 14 723	0.0851 ± 0.04	1.82 ± 0.05, 3.43 ± 0.02	39.08 ± 14.22, 28.27 ± 3.047
405	92	257 243.8 ± 42 907	0.0670 ± 0.05	1.69 ± 0.01, 3.43 ± 0.01	26.56 ± 17.50, 41.94 ± 14.22

non-local free charge carriers, and is consistent with fact that the DC and Drude-fitted conductivity of hexagonal $Ge_2Sb_2Te_5$ are also similar.[19]

The conductivity behavior at intermediate phases is also worth studying. In this case, when a constant voltage is applied to the PCM, the increase of current depends on the nucleation level (associated with the applied annealing temperature). If nuclei are not yet in physical contact (initial nucleation stage) such that they form a low resistance current path through the sample, the increase in current is small. When multiple crystallites meet each other (percolation) and form a continuous crystalline path between electrodes, the current immediately becomes much larger.[19] To analyze this mixed-phase regime, we examined a $Ge_3Sb_2Te_6$ sample annealed at 355 °C, representing an intermediate cubic-trigonal (polycrystalline) state. In this case, $\sigma_{DC}^{TDS} \approx 1854\ \sigma_{DC}^{4PP}$. This large discrepancy strongly suggests a scenario where the material contains partially crystallized regions without fully connected percolation paths. As a result, 4PP detects poor long-range DC transport, as carriers driven by low-frequency fields undergo significant scattering at grain boundaries. Contrarily, the latter are not a dominant factor at THz frequencies, as carriers can mode inside grains,[9] and THz-TDS remains sensitive to localized carrier motion within isolated crystalline domains, as discussed in previous works for other PCMs. For instance, the DC conductivity of a thin-film polycrystalline $Ge_2Sb_2Te_5$ sample, where grain boundary scattering significantly inhibits current flow, is much lower than the value determined by the Drude model.[19] The difference between the THz-TDS and DC measurements decreases with increasing annealing temperature because of the enhancement in grain size and the decrease of scattering at grain boundaries, as we observed for an annealing temperature of 405 °C, and in agreement with previous studies on $Ge_2Sb_2Te_5$.[9,19]

Finally, it is worth mentioning that THz transmission measurements (from which all optical and electrical properties were obtained) were performed at three different spots on each sample, allowing us to average out potential inhomogeneities, which can arise from nanoscale thickness variations, partial crystallization, and mixed-phase regions. Additionally, systematic errors arising from setup misalignment, particularly those caused by mechanical instabilities in the delay stage, cannot be ruled out. As an illustration of the characterization uncertainty induced by these factors, we quantified standard deviation values in the extracted transmittance, and complex refractive index of $Ge_3Sb_2Te_6$ over a Si substrate at 1 THz, which are included in Table 2, along with the corresponding mean values of these quantities. Standard deviation values for the full studied spectrum are shown in Fig. S2 of SI3 (SI).

Table 2 Numerically extracted optical constants at 1 THz for $Ge_3Sb_2Te_6$ samples (Si substrate) annealed at various temperatures. Each value is presented as the mean ± standard deviation across three measurement spots

Annealing temp. (°C)	Transmittance (%)	Refractive index (n)	Extinction coefficient (k)
As grown	99.3 ± 0.08	8.7 ± 3.20	0.2 ± 0.19
155	92.4 ± 0.13	9.5 ± 0.67	3.8 ± 0.25
205	71.7 ± 0.03	17.5 ± 3.11	12.7 ± 2.59
255	68.3 ± 0.24	21.5 ± 1.19	8.4 ± 0.77
305	46.4 ± 0.86	25.9 ± 1.08	18.4 ± 0.74
355	17.1 ± 0.69	40.8 ± 1.15	32.5 ± 1.95
405	8.6 ± 0.41	53.1 ± 1.72	51.7 ± 3.23

Conclusions

We have systematically investigated the effect of thermal annealing on the optical, electrical and conductive properties of a non-volatile chalcogenide compound $Ge_3Sb_2Te_6$ and compared its performance with the well-established $Ge_2Sb_2Te_5$ compound. Our results demonstrate that $Ge_3Sb_2Te_6$ exhibits lower losses compared to $Ge_2Sb_2Te_5$. Furthermore, the influence of the substrate on the optical properties is less pronounced for $Ge_3Sb_2Te_6$, whereas $Ge_2Sb_2Te_5$ shows significant substrate-dependent variations. Notably, the maximum annealing temperature for which $Ge_2Sb_2Te_5$ films did not exhibit spatial non-uniformity was limited to 305 °C, which constrains the maximum achievable refractive index. In contrast, $Ge_3Sb_2Te_6$ samples were studied for annealing temperatures up to 405 °C, with no signs of degradation. These results suggest that $Ge_3Sb_2Te_6$ could sustain even higher annealing temperatures, potentially leading to greater optical contrast and enhanced performance.

Author contributions

C. G.-M conceived and proposed the study. M. K. fabricated the samples at Nanophotonics Technology Center (NTC) of Universitat Politecnica de Valencia (UPV). M. K. Z. and J. A. A.-S. performed the THz-TDS transmission measurements at the NTC facility of UPV. M. K. Z. and D. O. D. Z. D. conducted the XRD and Raman spectroscopy measurements at the University of Valencia. K. K. carried out the Fourier transform analysis, implemented the required analytical and numerical computational techniques for data processing, extracted the optical properties, and performed material model fitting including optimizations of the Drude and Lorentz models. K. K. also validated the extracted parameters using electromagnetic wave simulation software, CST Studio Suite, conducted comparative analyses, and wrote the manuscript. B. V. and C. G.-M supervised the project and reviewed the manuscript.

Conflicts of interest

There are no conflicts to declare.

Data availability

Supplementary information: Comparison with previous reported data on the optical properties of Ge-Sb-Te compounds, DC electrical characterization, and measurement uncertainty quantification. See DOI: **https://doi.org/10.1039/d5tc01667c**.

Data for this article, including THz-TDS, Raman, and XRD data, are available at The Materials Data Facility at **https://doi.org/10.18126/1v02-w971**.

Acknowledgements

The authors wish to acknowledge support from the TERAOPTICS project (grant no: 956857) funded by the European Union's research and innovation program and projects PID2019-111339GBI00 and TED2021-132259B-I00 from the Agencia Estatal de Investigacion of the Spanish Ministerio de Ciencia e Innovacion. The authors would also like to thank Surya Revanth Ayyagari and Irmantas Kasalynas from FTMC, Lithuania, for their help in taking the optical images of the samples. Funding for open access charge: CRUE-Universitat Politècnica de València.

References

1 P. Jost, H. Volker, A. Poitz, C. Poltorak, P. Zalden, T. Schäfer, F. R. L. Lange, R. M. Schmidt, B. Holländer, M. R. Wirtssohn and M. Wuttig, *Adv. Funct. Mater.*, 2015, **25**, 6399–6406.

2 Z. Fang, R. Chen, B. Tossoun, S. Cheung, D. Liang and A. Majumdar, *APL Mater.*, 2023, **11**, 100603.

3 W. Zhang, A. Thiess, P. Zalden, R. Zeller, P. H. Dederichs, J.-Y. Raty, M. Wuttig, S. Blügel and R. Mazzarello, *Nat. Mater.*, 2012, **11**, 952–956.

4 V. Bragaglia, K. Holldack, J. E. Boschker, F. Arciprete, E. Zallo, T. Flissikowski and R. Calarco, *Sci. Rep.*, 2016, **6**, 28560.

5 T. Siegrist, P. Jost, H. Volker, M. Woda, P. Merkelbach, C. Schlockermann and M. Wuttig, *Nat. Mater.*, 2011, **10**, 202–208.

6 K. Shportko, S. Kremers, M. Woda, D. Lencer, J. Robertson and M. Wuttig, *Nat. Mater.*, 2008, **7**, 653–658.

7 Y. Zhang, C. Ríos, M. Y. Shalaginov, M. Li, A. Majumdar, T. Gu and J. Hu, *Appl. Phys. Lett.*, 2021, **118**, 210501.

8 P. Pitchappa, A. Kumar, S. Prakash, H. Jani, T. Venkatesan and R. Singh, *Adv. Mater.*, 2019, **31**, 1808157.

9 K. Makino, K. Kato, Y. Saito, P. Fons, A. V. Kolobov, J. Tominaga, T. Nakano and M. Nakajima, *J. Mater. Chem. C*, 2019, **7**, 8209–8215.

10 A. A. Gavdush, G. A. Komandin, V. V. Bukin, K. I. Zaytsev, D. S. Ponomarev, L. Tan, W. Huang and Q. Shi, *J. Appl. Phys.*, 2023, **134**, 085103.

11 K. Shportko, P. Zalden, A. Lindenberg, R. Rückamp and M. Grüninger, *Vib. Spectrosc.*, 2018, **95**, 51–56.

12 A.-K. U. Michel, D. N. Chigrin, T. W. W. Maß, K. Schönauer, M. Salinga, M. Wuttig and T. Taubner, *Nano Lett.*, 2013, **13**, 3470–3475.

13 A.-K. U. Michel, P. Zalden, D. N. Chigrin, M. Wuttig, A. M. Lindenberg and T. Taubner, *ACS Photonics*, 2014, **1**, 833–839.

14 J.-W. Park, S. H. Eom, H. Lee, J. L. F. Da Silva, Y.-S. Kang, T.-Y. Lee and Y. H. Khang, *Phys. Rev. B:Condens. Matter Mater. Phys.*, 2009, **80**, 115209.

15 W. Dong, H. Liu, J. K. Behera, L. Lu, R. J. H. Ng, K. V. Sreekanth, X. Zhou, J. K. W. Yang and R. E. Simpson, *Adv. Funct. Mater.*, 2018, **29**, 1806181.

16 M. Delaney, I. Zeimpekis, D. Lawson, D. W. Hewak and O. L. Muskens, *Adv. Funct. Mater.*, 2020, **30**, 2002447.

17 Z. Fang, R. Chen, V. Tara and A. Majumdar, *Sci. Bull.*, 2023, **68**, 783–786.

18 L. Duvillaret, F. Garet and J.-L. Coutaz, *IEEE J. Sel. Top. Quantum Electron.*, 1996, **2**, 739–746.

19 S. Raoux and M. Wuttig, *Phase Change Materials: Science and Applications*, Springer US, 2009.

20 Y. Zhang, C. Fowler, J. Liang, B. Azhar, M. Y. Shalaginov, S. Deckoff-Jones, S. An, J. B. Chou, C. M. Roberts, V. Liberman, M. Kang, C. Ríos, K. A. Richardson, C. Rivero-Baleine, T. Gu, H. Zhang and J. Hu, *Nat. Nanotechnol.*, 2021, **16**, 661–666.

21 Z. Sun, S. Kyrsta, D. Music, R. Ahuja and J. M. Schneider, *Solid State Commun.*, 2007, **143**, 240–244.

22 P. Němec, A. Moreac, V. Nazabal, M. Pavlišta, J. Přikryl and M. Frumar, *J. Appl. Phys.*, 2009, **106**, 103509.

23 K. Shportko, L. Revutska, O. Paiuk, J. Baran, A. Stronski, A. Gubanova and E. Venger, *Opt. Mater.*, 2017, **73**, 489–496.

24 Z. Xu, C. Chen, Z. Wang, K. Wu, H. Chong and H. Ye, *RSC Adv.*, 2018, **8**, 21040–21046.

25 R. De Bastiani, A. Piro, M. Grimaldi, E. Rimini, G. Baratta and G. Strazzulla, *Appl. Phys. Lett.*, 2008, **92**, 245205.

26 V. Bragaglia, F. Arciprete, A. M. Mio and R. Calarco, *J. Appl. Phys.*, 2018, **123**, 215304.

27 K. S. Andrikopoulos, S. N. Yannopoulos, G. A. Voyiatzis, A. V. Kolobov, M. Ribes and J. Tominaga, *J. Phys.: Condens. Matter*, 2006, **18**, 965–979.

28 I. Watanabe, S. Noguchi and T. Shimizu, *J. Non-Cryst. Solids*, 1983, **58**, 35–40.

29 O. Uemura, N. Hayasaka, S. Tokairin and T. Usuki, *J. Non-Cryst. Solids*, 1996, **205–207**, 189–193.

30 I. Kotsalas, D. Papadimitriou, C. Raptis, M. Vlcek and M. Frumar, *J. Non-Cryst. Solids*, 1998, **226**, 85–91.

31 K. Andrikopoulos, S. Yannopoulos, A. Kolobov, P. Fons and J. Tominaga, *J. Phys. Chem. Solids*, 2007, **68**, 1074–1078.

32 P. Němec, V. Nazabal, A. Moreac, J. Gutwirth, L. Beneš and M. Frumar, *Mater. Chem. Phys.*, 2012, **136**, 935–941.

33 H. Peng, K. Cil, A. Gokirmak, G. Bakan, Y. Zhu, C. Lai, C. Lam and H. Silva, *Thin Solid Films*, 2012, **520**, 2976–2978.

34 G. C. Sosso, S. Caravati, R. Mazzarello and M. Bernasconi, *Phys. Rev. B:Condens. Matter Mater. Phys.*, 2011, **83**, 134201.

35 A. Shalini, Y. Liu, F. Katmis, W. Braun, G. P. Srivastava and R. J. Hicken, *J. Appl. Phys.*, 2015, **117**, 025306.

36 F. Kadlec, C. Kadlec, P. Kužel and J. Petzelt, *Phys. Rev. B:Condens. Matter Mater. Phys.*, 2011, **84**, 205209.

37 R. Ulbricht, E. Hendry, J. Shan, T. F. Heinz and M. Bonn, *Rev. Mod. Phys.*, 2011, **83**, 543–586.

38 H. J. Joyce, J. L. Boland, C. L. Davies, S. A. Baig and M. B. Johnston, *Semicond. Sci. Technol.*, 2016, **31**, 103003.

39 F. Kadlec, C. Kadlec and P. Kužel, *Solid State Commun.*, 2012, **152**, 852–855.

40 H. Zhu, J. Li, X. Lu, Q. Shi, L. Du, Z. Zhai, S. Zhong, W. Wang, W. Huang and L. Zhu, *J. Phys. Chem. Lett.*, 2022, **13**, 947–953.

41 H.-K. Lyeo, D. G. Cahill, B.-S. Lee, J. R. Abelson, M.-H. Kwon, K.-B. Kim, S. G. Bishop and B.-K. Cheong, *Appl. Phys. Lett.*, 2006, **89**, 151904.

42 I. Miccoli, F. Edler, H. Pfnür and C. Tegenkamp, *J. Phys.: Condens. Matter*, 2015, **27**, 223201.